

Synthesis, Characterisation and Evaluation of IrO₂ Based Binary Metal Oxide Electrocatalysts for Oxygen Evolution Reaction

C. Felix, T. Maiyalagan^{*}, S. Pasupathi^{*}, B. Bladergroen, V. Linkov

South African Institute for Advanced Materials Chemistry (SAIAMC), University of the Western Cape, Modderdam Road, Bellville 7535, Cape Town, South Africa

^{*}E-mail: spasupathi@uwc.ac.za; maiyalagan@gmail.com

Received: 13 June 2012 / Accepted: 29 September 2012 / Published: 1 December 2012

IrO₂, Ir_xRu_{1-x}O₂, Ir_xSn_{x-1}O₂ and Ir_xTa_{x-1}O₂ ($1 \geq x \geq 0.7$) were synthesized, characterised and evaluated as electrocatalysts for the oxygen evolution reaction in solid polymer electrolyte electrolyzers. The electrocatalysts were synthesised by adapting the Adams fusion method. The physical properties of the electrocatalysts were characterised by scanning electron microscopy, transmission electron microscopy and x-ray diffraction. Electrochemical activity of the electrocatalysts toward the oxygen evolution reaction was evaluated by cyclic voltammetry and chronoamperometry. X-ray diffraction revealed no phase separation when RuO₂ or SnO₂ was introduced into the IrO₂ lattice suggesting that solid solutions were formed. Transmission electron microscope analysis revealed nanosize particles for all synthesised metal oxides. Crystallinity increased with the addition of RuO₂ and SnO₂ while a suppression of crystal growth was observed with the addition of Ta₂O₅ to IrO₂. Chronoamperometry revealed that the addition of all the secondary metal oxides to IrO₂ resulted in improved catalytic performance. Ir_{0.7}Ru_{0.3}O₂ was identified as the most promising electrocatalyst for the oxygen evolution reaction.

Keywords: Adams fusion method, Anodic electrocatalyst, Oxygen evolution reaction, Solid polymer electrolyte, Water electrolysis.

1. INTRODUCTION

Solid polymer electrolyte (SPE) or commonly known as proton exchange membrane (PEM) electrolyzers have in recent years received considerable interest as a production method for carbon free hydrogen [1 - 3]. SPE electrolyzers are well suited for water electrolysis using intermittent power sources and have been identified by the European Commission as a key technology to transform

renewable electricity into hydrogen and oxygen [4]. The main drawback at present is the high cost associated with the SPE electrolyser components such as the expensive precious metal electrocatalysts and proton conducting membranes [5, 6]. One way to reduce the cost of the SPE electrolyser is by improving the specific performance and durability of the noble metal electrocatalysts. The oxygen evolution electrode (anode) is the greatest source of overpotential of the system at typical operating current density [2, 6] therefore the anodic electrocatalyst needs to be highly stable and active under the operating conditions [7]. IrO₂ is commonly employed as the anodic electrocatalyst as it exhibits a high corrosion resistance to the oxygen evolution reaction (OER) in a strong acidic environment [7, 8]. IrO₂ is scarce and very expensive [9], adding significantly to the cost of the SPE electrolyser system. Since there is still no non-metal electrocatalyst with satisfactory activity and durability, it becomes important to improve both the activity and durability of the IrO₂ electrocatalyst. The most common method of enhancing the electrochemical properties of the IrO₂ electrocatalyst is by insertion of other metal oxides into the IrO₂ lattice. In this study, IrO₂, Ir_xRu_{1-x}O₂, Ir_xSn_{x-1}O₂ and Ir_xTa_{x-1}O₂ ($1 \geq x \geq 0.7$) were synthesised and characterised as suitable anodic electrocatalysts for the SPE electrolyser. RuO₂ is known to be the most active towards the OER but suffers from instability, and should thus be stabilised with another metal oxide such as IrO₂ or SnO₂ [10, 11]. Corrosion of Ru proceeds via RuO₄ and is directly coupled to oxygen evolution via this common intermediate. The stabilisation of Ru by Ir has been explained on the basis of shifted oxidation potentials and surface segregation [12]. IrO₂ thus stabilises RuO₂ by preventing its oxidation to the soluble RuO₄ [13]. Ir-Ru mixed oxides are known to have superior catalytic and stability properties with respect to Ru-Ti mixed oxide electrodes [14]. Ta is a well known addition to the dimensionally stable anode (DSA) electrodes and Ir-Ta oxides have been suggested to be an efficient catalyst for the OER in acidic media due to the high activity and corrosion resistance [2]. The IrO₂-Ta₂O₅ system as DSAs is a promising catalyst in various electrochemical industries, such as cleaning of waste water and electrowinning (electro-extraction) of metals, where oxygen evolution is the main anodic reaction. However Ta₂O₅ is mainly added to improve the service life of IrO₂, which is the active and most expensive component [15]. IrO₂-Ta₂O₅ with the composition of 70 % IrO₂ and 30% Ta₂O₅ has been previously verified to be the best combination in binary metal oxide systems in present commercial applications [16]. Sn was selected on the basis of its high chemical and mechanical stability as well as its lower cost than the expensive noble metals [17]. The Adams fusion method was adapted to synthesise the Ir based metal oxides and the electrocatalytic activities were evaluated by cyclic voltammetry (CV) and chronoamperometry (CA). Physical characterisation was performed by scanning electron microscope (SEM), transmission electron microscope (TEM) and x-ray diffraction (XRD).

2. EXPERIMENTAL DETAILS

2.1 Preparation of the catalyst

The Adams fusion method, first described by R. Adams and R.L. Shriner [18], entails the fusion of the metal chloride precursor with NaNO₃ in air at elevated temperatures. The method has

since been used to synthesise various noble metal oxides [15, 17-19]. H_2IrCl_6 (SA precious metals, South Africa), RuCl_3 , $\text{SnCl}_2 \cdot 2\text{H}_2\text{O}$ and TaCl_5 (Alfa Aesar, Johnson Matthey) were used as catalyst precursors to synthesise the electrocatalysts. The catalyst precursor(s) were dissolved in 10 ml isopropanol (Alfa Aesar, Johnson Matthey) until a metal concentration of 3.5×10^{-2} M was achieved and magnetically stirred for 90 minutes. For each type of binary metal oxide system the second metal (Sn, Ru or Ta) was added in a concentration of 5–30 mol % to Ir. Five grams of finely ground NaNO_3 (Holpro Fine Chemicals, South Africa) was added to the solution, which was then further stirred for 30 minutes. The mixture was then dried in an oven for 30 minutes. The dried catalyst precursor/salt mixture was then reacted in a furnace for 120 minutes at 350 °C. No additional annealing step followed to limit the sintering of the nanosize particles. The obtained metal oxide was cooled and washed with ultrapure water to remove the unreacted NaNO_3 . The final step was to dry the metal oxide in an oven for 120 minutes at 100 °C.

2.2 Preparation of the working electrode

A predetermined size of Ti mesh (Bekinit K.K, Japan) was etched and cleaned by boiling in oxalic acid (NT Laboratory Supplies) for 12 minutes. Catalyst inks were prepared by mixing together the synthesised metal oxides, 5 wt% Nafion solution (Aldrich) and ultrapure water in a ratio of 1:6:2. A measured volume of isopropanol was added to serve as dispersion medium. The mixture was ultrasonically dispersed for 30 minutes. An airbrush with N_2 propulsion was used to spray the catalyst ink (1 mg cm^{-2}) onto the pre-treated Ti mesh. The catalyst ink was thoroughly dried between each layer sprayed to prevent agglomeration of the electrocatalytic particles. Spraying of the catalyst layer was followed by spraying a Nafion layer (1 mg cm^{-2}). The working electrode was cut out with a punch and had an area of 0.785 cm^2 .

2.3 Physical characterisation

Physical phases and structures of the electrocatalysts were characterised by X-ray diffraction (XRD) employing the Bruker AXS D8 Advance diffractometer using Cu K_α radiation ($\lambda = 1.5406 \text{ \AA}$) operating at 40 kV and 40 mA. Scanning electron micrographs were obtained with the Hitachi X-650 SEM using GENESIS software, working at 25 keV. Transmission electron micrographs were obtained using a Tecnai G² F20 X-Twin Mat200 kV Field Emission TEM, operating at 200 kV.

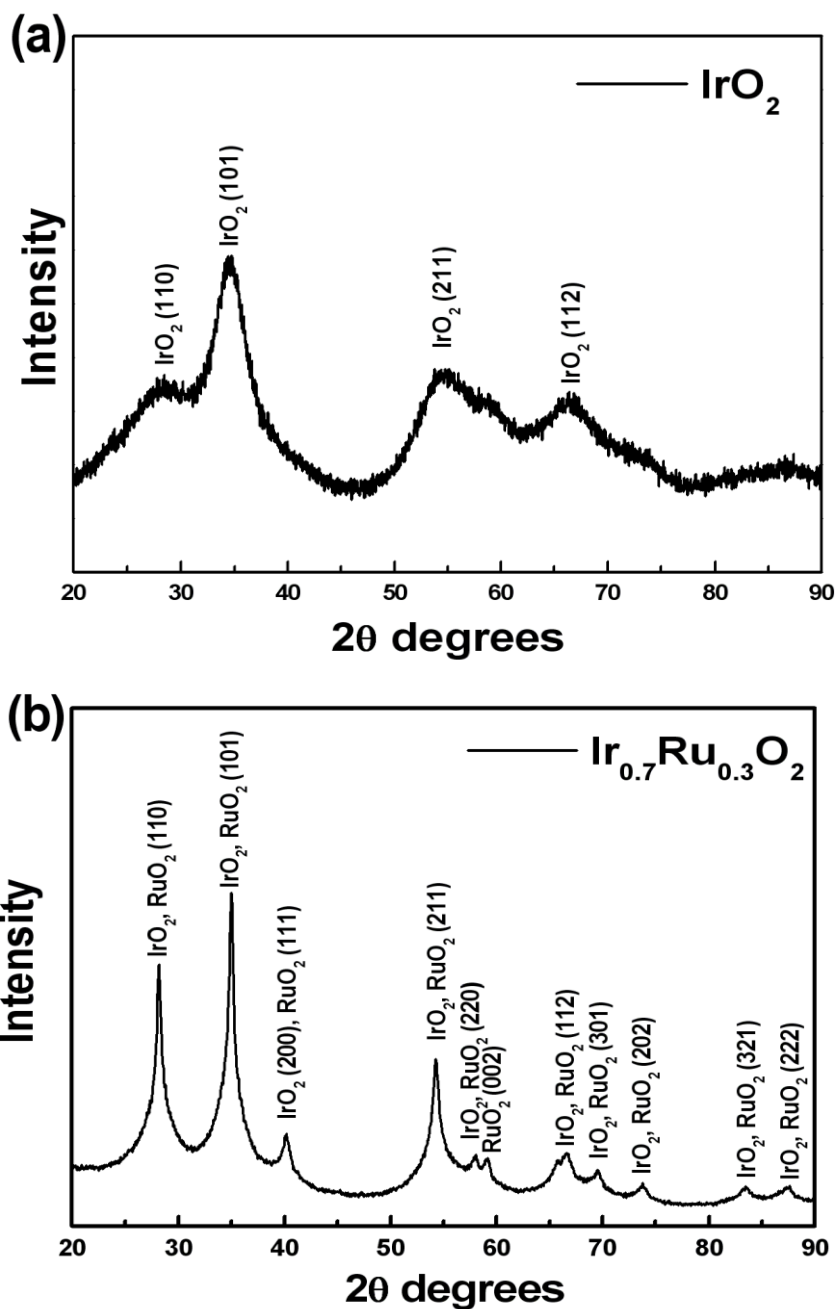
2.4 Electrochemical characterisation

Electrochemical analyses were performed in a standard three-electrode cell at 25 °C and atmospheric pressure. The Ti mesh working electrode (as described in earlier), a 3M Ag/AgCl reference electrode, a Pt mesh counter electrode and a 0.5 M H_2SO_4 electrolyte solution was used. Autolab potentiostat PGSTAT20 (Eco-Chemie) was used for CV and CA analyses to evaluate the electrocatalytic activity of the synthesised electrocatalysts towards the OER. The electrolyte solution

was purged with N_2 for 30 minutes before performing electrochemical measurements. CV was performed by cycling the potential from -0.2 to +1.2 V at a potential sweep rate of 50 mV s^{-1} . CA was performed by stepping the potentials from 1.2 to 1.6 V and measuring the current (mA) response as a function of time. Each potential step was performed for 30 minutes. All potentials are reported versus the 3M Ag/AgCl electrode.

3. RESULTS AND DISCUSSION

3.1 Physical characterisation



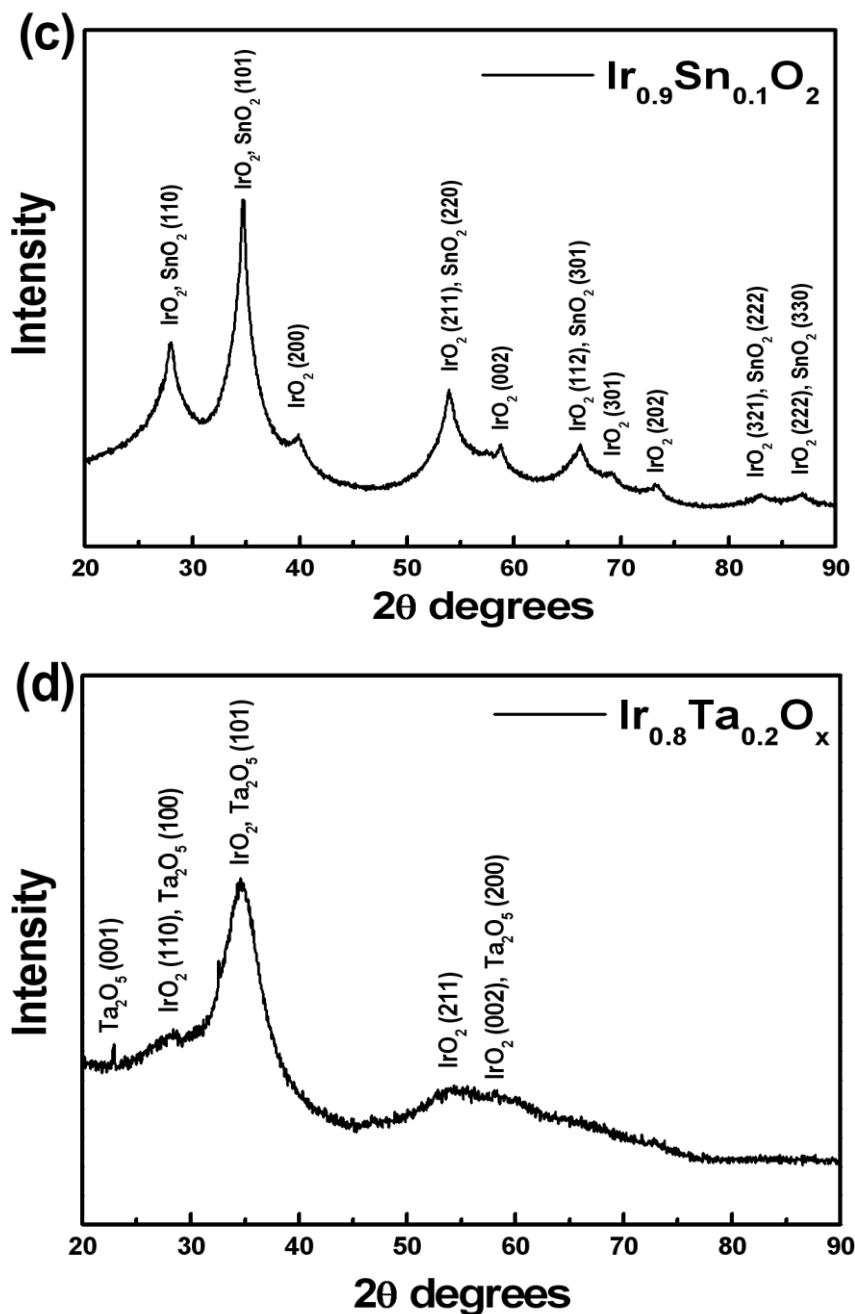


Figure 1. XRD patterns of (a) IrO_2 (b) $\text{Ir}_{0.7}\text{Ru}_{0.3}\text{O}_2$ (c) $\text{Ir}_{0.9}\text{Sn}_{0.1}\text{O}_2$ and (d) $\text{Ir}_{0.8}\text{Ta}_{0.2}\text{O}_x$.

Fig. 1 shows the XRD patterns of IrO_2 and the best performing electrocatalysts (established by CA analysis) of the three metal oxide combinations i.e. $\text{Ir}_{0.7}\text{Ru}_{0.3}\text{O}_2$, $\text{Ir}_{0.9}\text{Sn}_{0.1}\text{O}_2$ and $\text{Ir}_{0.8}\text{Ta}_{0.2}\text{O}_x$. The XRD analysis of IrO_2 (Fig. 1a) revealed a rutile oxide characterised by an amorphous phase which is known to consist of smaller particles. Calculated from the 101 phase using the Scherrer formula, the average particle size was estimated to be 3.5 nm. No metallic Ir was observed. The XRD analysis of $\text{Ir}_{0.7}\text{Ru}_{0.3}\text{O}_2$ (Fig. 1b) revealed a crystalline structure assigned to tetragonal rutile. Sharper peaks were observed in comparison to pure IrO_2 which indicates an increase in the particle size. The single peaks observed at the 110 and 101 phases ($2\theta = 28^\circ$ and 35° respectively) suggests that $\text{Ir}_{0.7}\text{Ru}_{0.3}\text{O}_2$ is a solid

solution of IrO_2 and RuO_2 . This observation is consistent with other reports [8, 9, and 13]. The addition of RuO_2 to IrO_2 resulted in an increase in the 110 phase (a stable surface of IrO_2) which may lead to a synergistic effect. Although it is known that IrO_2 and RuO_2 can form stable solid solutions, the presence of multiple rutile phases should not be ruled out. The Hume–Rothery theory states that it is possible to form a continuous solid solution of IrO_2 and RuO_2 , where Ru^{4+} and Ir^{4+} share the same site on the cationic sub-lattice of a tetragonal (rutile-like) phase [20]. The higher degree of crystallisation observed for $\text{Ir}_{0.7}\text{Ru}_{0.3}\text{O}_2$ in comparison to pure IrO_2 may be attributed to the fact that RuO_2 crystallises at a lower temperature than IrO_2 [21]. Calculated from the 110 and 101 phases using the Scherrer formula, the average particle size for $\text{Ir}_{0.7}\text{Ru}_{0.3}\text{O}_2$ was estimated at 11 nm. The presence of metallic Ir and Ru was not observed.

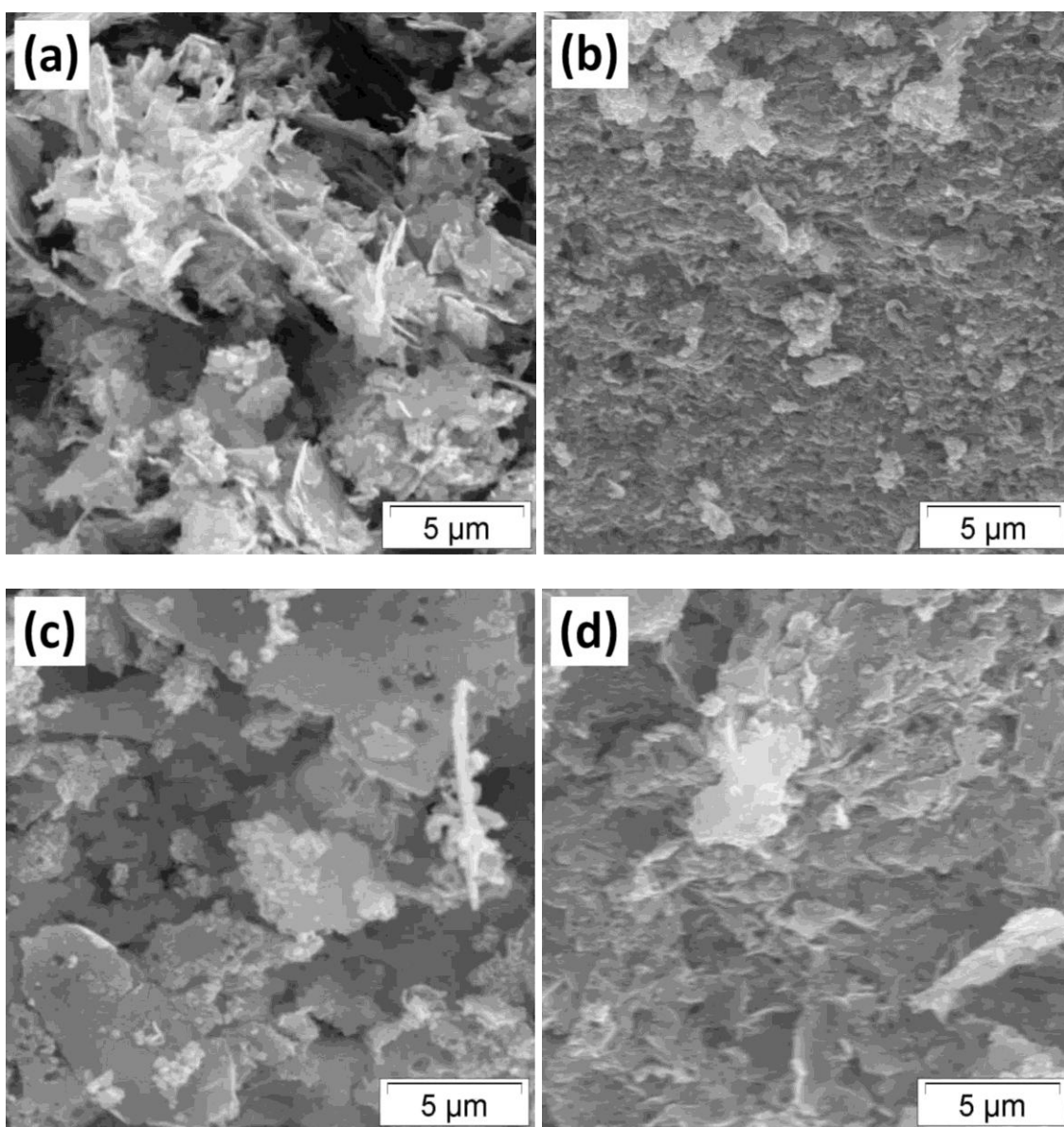


Figure 2. SEM images of (a) IrO_2 (b) $\text{Ir}_{0.7}\text{Ru}_{0.3}\text{O}_2$ (c) $\text{Ir}_{0.9}\text{Sn}_{0.1}\text{O}_2$ and (d) $\text{Ir}_{0.8}\text{Ta}_{0.2}\text{O}_x$.

XRD analysis of $\text{Ir}_{0.9}\text{Sn}_{0.1}\text{O}_2$ (Fig. 1c) revealed a rutile-type oxide with single peaks observed at the 110 and 101 phases ($2\theta = 28^\circ$ and 35° respectively) which suggests that $\text{Ir}_{0.9}\text{Sn}_{0.1}\text{O}_2$ is a solid solution of IrO_2 and SnO_2 . The addition of SnO_2 to IrO_2 resulted in an increase in the 110 phase (a stable surface of IrO_2) which may lead to a synergistic effect. Mayousse *et al.* [9] also observed the formation of a solid solution between IrO_2 and SnO_2 . They suggested that IrO_2 and SnO_2 crystallised in the same tetragonal structure due to the comparable atomic radii of Ir and Sn. However the presence of two phases should not be ruled out. Marshall *et al.* [22] used profiling of the XRD patterns and suggested that the XRD patterns were a mixture of two highly dispersed rutile oxide phases. The presence of multiple phases and the lack of a single solid solution phase were suggested to arise from the poor interaction of the precursors during the initial stages of the reaction. It was assumed that SnO_2 formed first since there is a significant difference in ΔG_f^0 for IrO_2 and SnO_2 (-510 kJ mol^{-1} [23] and $-186.5 \text{ kJ mol}^{-1}$ [24], respectively). Calculated from the 110 and 101 phases using the Scherrer formula, the average particle size for $\text{Ir}_{0.9}\text{Sn}_{0.1}\text{O}_2$ was estimated at 6.5 nm. The presence of metallic Ir and Sn was not observed.

XRD analysis of $\text{Ir}_{0.8}\text{Ta}_{0.2}\text{O}_x$ (Fig. 1d) revealed a slight decrease in the 110 phase of IrO_2 and a slight increase in the 002 (one of the non-close-packed planes of the Ir atom) phase which is consistent with what is reported in the literature [25]. This could be explained by the stabilisation effect that Ta has on the Ir component in the non-close-packed plane [14]. XRD analysis further revealed mainly an amorphous phase which is consistent with the results of Di Blasi *et al* [26]. Calculated from 101 phase using the Scherrer formula, the average particle size for $\text{Ir}_{0.8}\text{Ta}_{0.2}\text{O}_x$ was estimated at 3 nm. The addition of Ta_2O_5 is known to suppress the crystallisation of IrO_2 [15]. Ta was found to be present in the +5 oxidation state; consistent to what was reported previously [2]. The presence of metallic Ir and Ta was not observed.

Fig. 2 shows the SEM images of IrO_2 and the best performing electrocatalysts (established by CA analysis) of the three metal oxide combinations i.e. $\text{Ir}_{0.7}\text{Ru}_{0.3}\text{O}_2$, $\text{Ir}_{0.9}\text{Sn}_{0.1}\text{O}_2$ and $\text{Ir}_{0.8}\text{Ta}_{0.2}\text{O}_x$. Particle formation and sizes could not be defined from the SEM images. The SEM image of IrO_2 (Fig. 2a) shows micrometer size flake shaped aggregates whereas $\text{Ir}_{0.7}\text{Ru}_{0.3}\text{O}_2$ (Fig. 2b), $\text{Ir}_{0.9}\text{Sn}_{0.1}\text{O}_2$ (Fig. 2c) and $\text{Ir}_{0.8}\text{Ta}_{0.2}\text{O}_x$ (Fig. 2d) exhibited sheet like porous morphology. From the SEM images, it appears that the addition of the secondary metal oxides to IrO_2 resulted in larger aggregate sizes.

Fig. 3 shows the TEM images of IrO_2 and the best performing electrocatalysts (established by CA analysis) of the three metal oxide combinations i.e. $\text{Ir}_{0.7}\text{Ru}_{0.3}\text{O}_2$, $\text{Ir}_{0.9}\text{Sn}_{0.1}\text{O}_2$ and $\text{Ir}_{0.8}\text{Ta}_{0.2}\text{O}_x$. TEM analysis of IrO_2 (Fig. 3a) revealed an amorphous phase consisting of nanoparticles with an average size of about 4.5 nm. TEM analysis of $\text{Ir}_{0.7}\text{Ru}_{0.3}\text{O}_2$ (Fig. 3b) revealed an amorphous phase consisting of smaller particles and a crystalline phase consisting of larger pin shaped particles of up to 80 nm in length. The larger pin shaped particles formed due to the crystallisation of RuO_2 as was revealed by XRD. TEM analysis of $\text{Ir}_{0.9}\text{Sn}_{0.1}\text{O}_2$ (Fig. 3c) revealed an amorphous phase consisting of smaller particles and a crystalline phase consisting of larger needle shaped particles of up to 50 nm in length. The larger needle shaped particles formed due to the crystallisation of SnO_2 as was revealed by XRD. From literature [22, 27], a slight increase in particle size was observed as the SnO_2 content was increased. The slight increase in particle size can be expected since the slightly larger Sn^{4+} ions (0.083 nm) are substituting the smaller Ir^{4+} ions (0.077 nm) in the IrO_2 lattice [28]. TEM analysis of

$\text{Ir}_{0.8}\text{Ta}_{0.2}\text{O}_x$ (Fig. 3d) revealed uniformly distributed nanosize particles with an average size of 3.5 nm. The most important enhancing effect that the addition of Ta_2O_5 to IrO_2 has is mainly related to the reduction of the particle size [15].

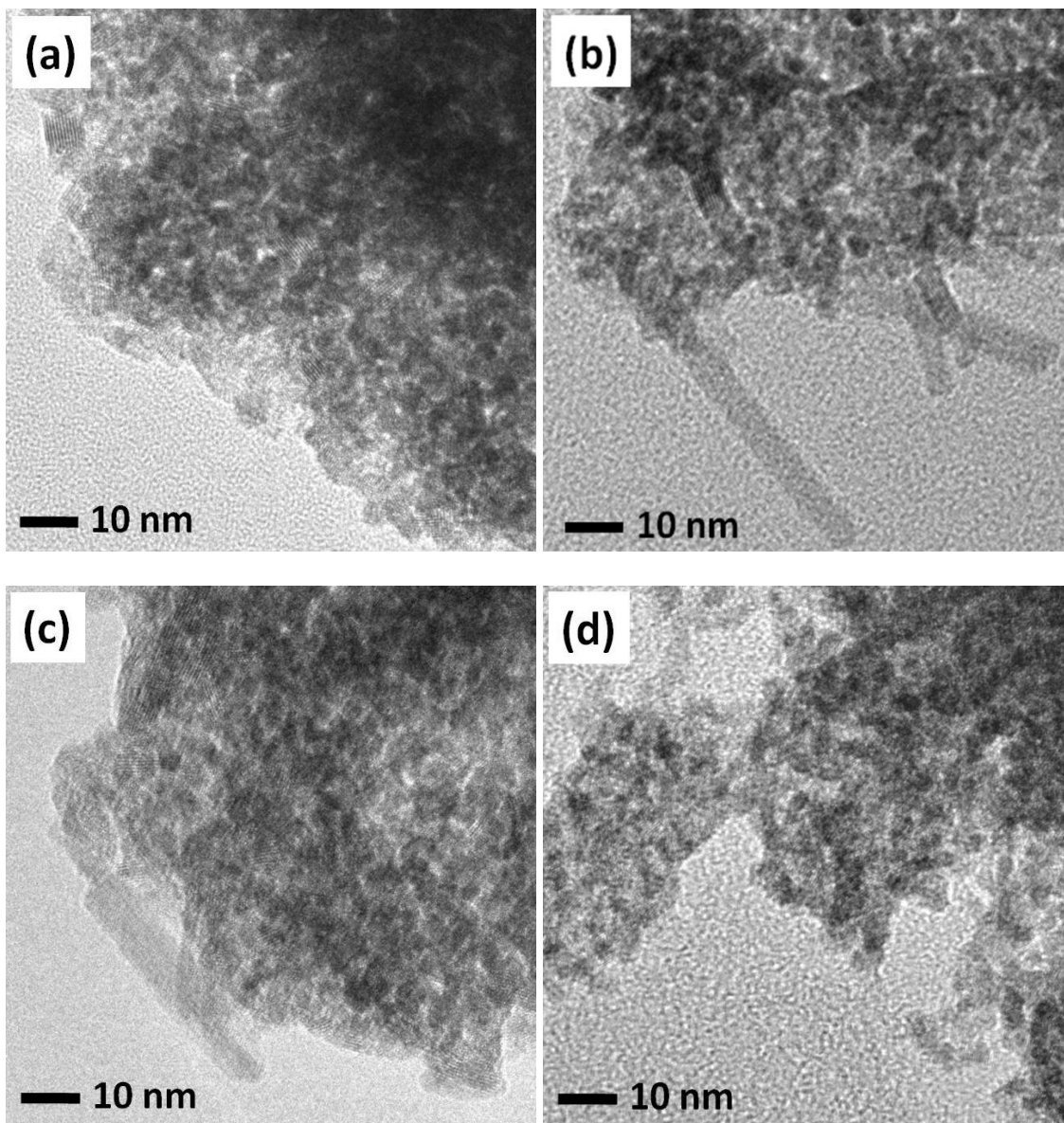


Figure 3. TEM images of (a) IrO_2 (b) $\text{Ir}_{0.7}\text{Ru}_{0.3}\text{O}_2$ (c) $\text{Ir}_{0.9}\text{Sn}_{0.1}\text{O}_2$ and (d) $\text{Ir}_{0.8}\text{Ta}_{0.2}\text{O}_x$.

3.2 Electrochemical characterisation

Fig. 4 shows the CV analysis for IrO_2 and the best performing electrocatalysts (as established by CA analysis) of the three metal oxide combinations i.e. $\text{Ir}_{0.7}\text{Ru}_{0.3}\text{O}_2$, $\text{Ir}_{0.9}\text{Sn}_{0.1}\text{O}_2$ and $\text{Ir}_{0.8}\text{Ta}_{0.2}\text{O}_x$. The potential was cycled from -0.2 to +1.2 V (vs. 3M Ag/AgCl electrode) at a potential sweep rate of 50 mV s^{-1} in 0.5M H_3SO_4 solution. The voltammetric curve for IrO_2 (Fig. 4a) shows two peaks at about 0.4 and 1 V which are located in the redox transition region [5]. The peaks at 0.4 and 1V have

been assigned to redox couples Ir (III)/Ir (IV) and Ir (IV)/Ir (VI), respectively. There is a lack of symmetry along the potential axis especially in the region of the Ir (IV)/Ir (VI) redox couple which is probably due to sluggish electrode kinetics.

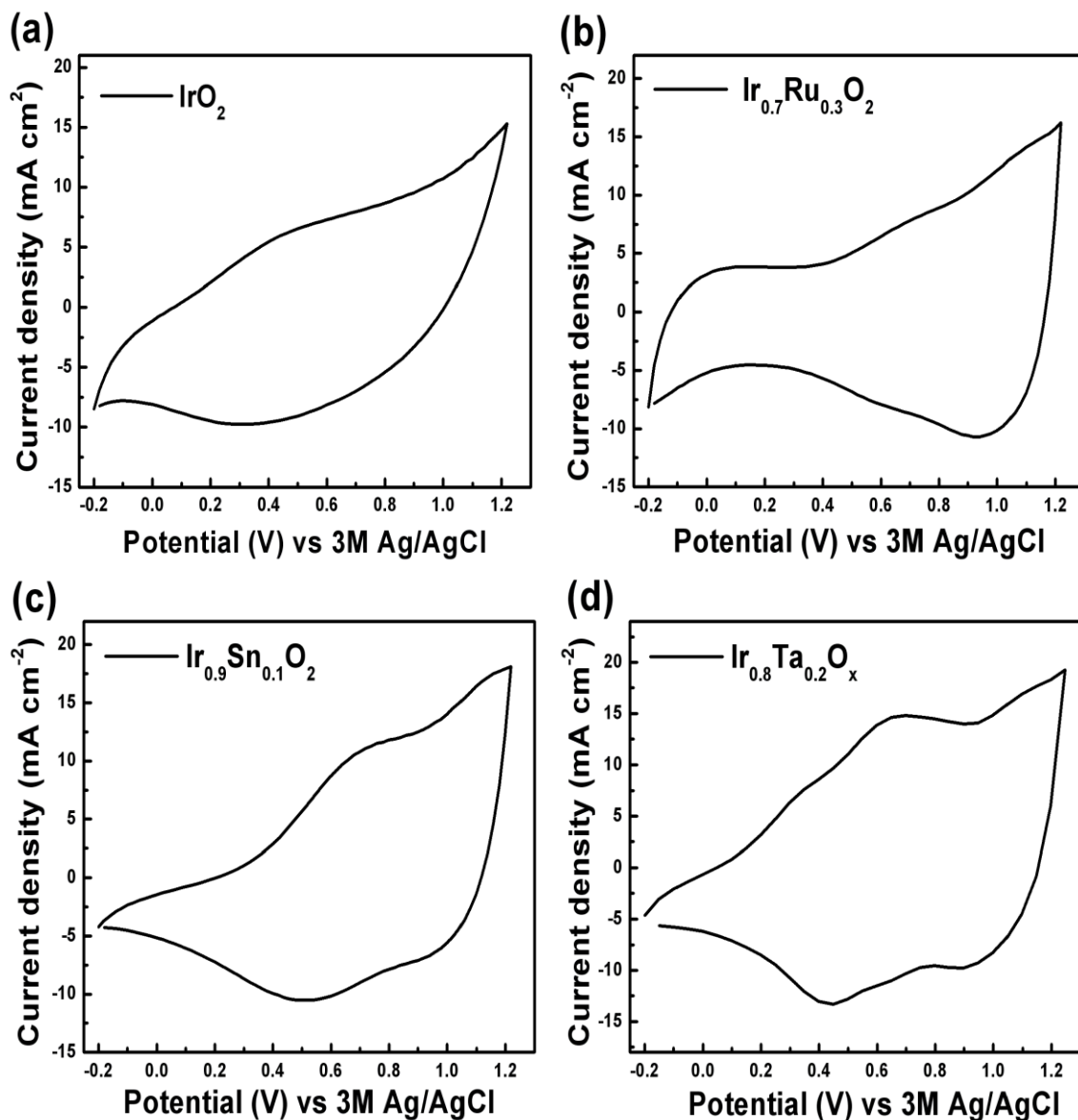


Figure 4. Cyclic voltammograms of (a) IrO₂ (b) Ir_{0.7}Ru_{0.3}O₂ (c) Ir_{0.9}Sn_{0.1}O₂ and (d) Ir_{0.8}Ta_{0.2}O_x at 50 mVs⁻¹.

Furthermore the peaks are broad and not well depicted suggesting the existence of a variety of active surface sites with different formal potentials which is consistent with an amorphous state of IrO₂ [29]. The voltammetric curve for Ir_{0.7}Ru_{0.3}O₂ (Fig. 4b) shows a positive potential shift for the redox transition region in comparison to pure IrO₂. The peak at about 0.6 and 0.95V was assigned to the redox transition couples of the Ru(III)/Ru(IV) and Ru(IV)/Ru(VI) respectively. The voltammogram displays reversible charge transfer transition in the O₂ evolution region which suggests an

improvement in electrode kinetics in comparison to pure IrO_2 . At about -0.1V there is a noticeable peak due to hydrogen adsorption which is commonly associated with the presence of a metallic species since hydrogen is not known to easily adsorb onto an oxide surface [29]. However, no metallic Ir or Ru was observed with XRD analysis. The voltammetric curve for $\text{Ir}_{0.9}\text{Sn}_{0.1}\text{O}_2$ (Fig. 4c) exhibits a shape similar to that of pure IrO_2 with a positive potential shift of the redox transition region which is observed between 0.65 and 1.1V . The peak at about 0.65V can be assigned to the Ir(III)/Ir(IV) couple since the electrode response is strongly dominated by the Ir component [27]. The voltammogram shows good reversibility in the O_2 evolution region suggesting improved electrode kinetics in comparison to pure IrO_2 . The voltammetric curve for $\text{Ir}_{(0.8)}\text{Ta}_{(0.2)}\text{O}_x$ (Fig. 4d) displays two peaks at 0.7 and 1.1V . The peak at about 0.7V is attributed to the Ir(III)/Ir(IV) couple which suggests that the surface electrochemistry is governed by the active component of IrO_2 [30]. The voltammogram shows good reversibility in the O_2 evolution region suggesting improved electrode kinetics in comparison to pure IrO_2 . CV was also used to investigate the electrochemical activities of the oxides which are related to the number of active sites accessible to the electrolyte solution [31]. The anodic charge, q_a , due to double layer charging and surface redox transitions, is proportional to the active site surface concentration [32].

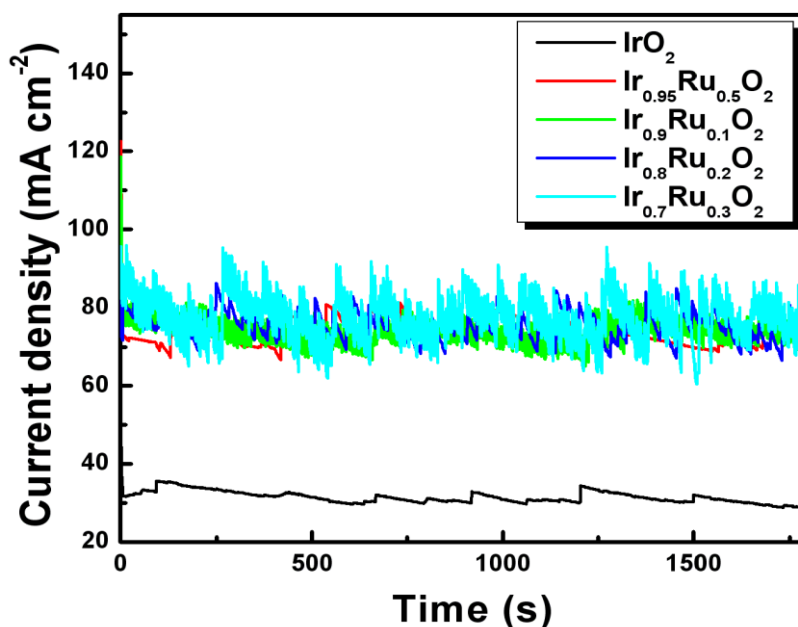


Figure 5. Chronoamperometric measurements of IrO_2 and $\text{Ir}_x\text{Ru}_{1-x}\text{O}_2$ ($1 \geq x \geq 0.7$) at 1.6V .

The q_a for the electrodes was obtained by integration of the voltammetric curves in the range between H_2 and O_2 gas evolution. The q_a values for IrO_2 , $\text{Ir}_{0.7}\text{Ru}_{0.3}\text{O}_2$, $\text{Ir}_{0.9}\text{Sn}_{0.1}\text{O}_2$ and $\text{Ir}_{0.8}\text{Ta}_{0.2}\text{O}_x$ are 144 , 185 , 180 and 274mC cm^{-2} , respectively. The mixed oxides show higher q_a than for pure IrO_2 indicating that Ru, Sn and Ta have a positive effect on the active area of the mixed oxide electrodes. J-M Hu *et al.* [33] observed that the voltammetric charge significantly varies with the Ta composition and that $20\text{ mol } \%$ Ta addition shows a significantly higher charge value than that of pure IrO_2 . The

higher q_a for $\text{Ir}_{0.8}\text{Ta}_{0.2}\text{O}_x$ may also be due to the smaller particle sizes as was revealed by TEM and XRD. De Pauli *et al.* [34] suggested that the sharp decrease in charge value as the electrode surface composition reached 100 mol % IrO_2 was due to diminution or a reduction of the surface area.

Fig. 5 shows the CA analysis of the $\text{Ir}_x\text{Ru}_{1-x}\text{O}_2$ ($1 \geq x \geq 0.7$) electrocatalysts performed at 1.6 V for 30 minutes. CA revealed the best electrocatalytic activity towards the OER for $\text{Ir}_{0.7}\text{Ru}_{0.3}\text{O}_2$. Electrocatalytic activity towards the OER increased as the RuO_2 content was increased. This observation is consistent with an improvement in the oxide activity due to the larger exchange current density of RuO_2 compared to that IrO_2 [2]. The catalytic activity of $\text{Ir}_{0.7}\text{Ru}_{0.3}\text{O}_2$ was significantly higher than that of pure IrO_2 . The addition of RuO_2 to IrO_2 was reported to result in a significant reduction in the overpotential [9]. The addition of RuO_2 of up to 80 mol% was also reported to yield an electrocatalyst with high electrochemical activity while displaying good stability under the OER [8]. The combination of RuO_2 and IrO_2 could thus facilitate a reduction in the required electrocatalyst loading as well as a direct material cost reduction considering that Ir is more expensive than Ru.

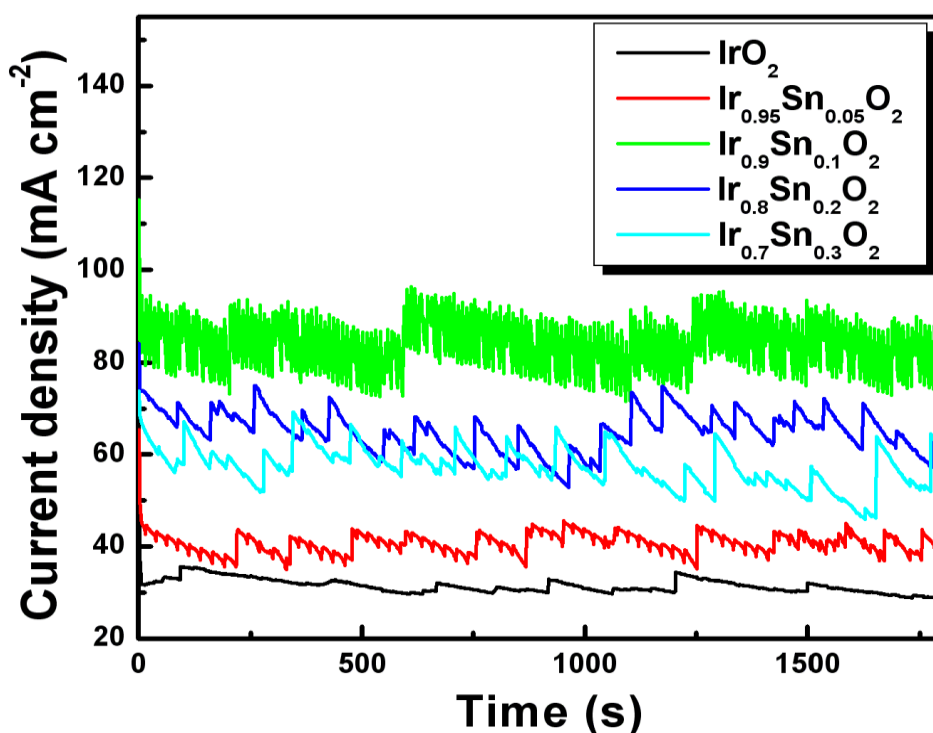


Figure 6. Chronoamperometric measurements of IrO_2 and $\text{Ir}_x\text{Sn}_{x-1}\text{O}_2$ ($1 \geq x \geq 0.7$) at 1.6 V.

Fig. 6 shows the CA analysis of the $\text{Ir}_x\text{Sn}_{x-1}\text{O}_2$ ($1 \geq x \geq 0.7$) electrocatalysts performed at 1.6 V for 30 minutes. CA revealed the best electrocatalytic activity towards the OER for $\text{Ir}_{0.9}\text{Sn}_{0.1}\text{O}_2$. A significant increase in electrocatalytic activity was observed as a Sn content of 10 mol% was reached which is consistent with a higher q_a value obtained from CV for $\text{Ir}_{0.9}\text{Sn}_{0.1}\text{O}_2$ as compared to pure IrO_2 . Further addition of Sn resulted in a rapid decrease in the oxide performance. However, CA analysis still revealed an improved performance for all IrO_2 - SnO_2 electrocatalysts in comparison to pure IrO_2 .

Xu *et al.* [1] reported similar behavior for their $\text{RuO}_2\text{-SnO}_2$ electrocatalysts where the catalytic activity initially increased followed by a dramatic decrease as the Sn content was increased. Marshall *et al.* [27] reported a 10 – 15% decrease in the total active area for SnO_2 contents of 20 – 30 mol% but also observed a better cell performance for $\text{Ir}_{0.8}\text{Sn}_{0.2}\text{O}_2$ as compared to pure IrO_2 at 25°C [11]. Xu *et al.* [35] observed that at low SnO_2 contents the IrO_2 particles were well dispersed but at higher SnO_2 contents the active surface area of IrO_2 decreased due to an increase in the average particle size.

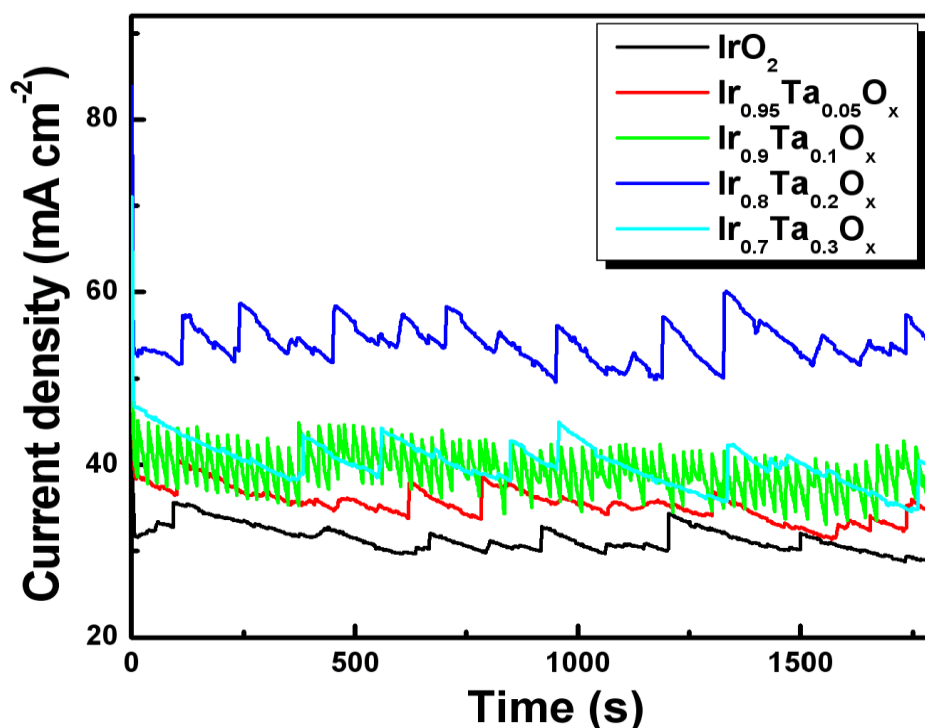


Figure 7. Chronoamperometric measurements of IrO_2 and $\text{Ir}_x\text{Ta}_{x-1}\text{O}_2$ ($1 \geq x \geq 0.7$) at 1.6 V.

Fig. 7 shows the CA analysis of the $\text{Ir}_x\text{Ta}_{x-1}\text{O}_2$ ($1 \geq x \geq 0.7$) electrocatalysts performed at 1.6 V for 30 minutes. The best catalytic activity towards the OER was observed for $\text{Ir}_{0.8}\text{Ta}_{0.2}\text{O}_x$. An increase in electrocatalytic activity was observed as the Ta content was increased up to 20 mol% followed by a decrease in electrocatalytic activity as the Ta content reached 30 mol%. The addition of Ta_2O_5 to IrO_2 was reported to increase the resistivity by 2 orders of magnitude by the time the composition reached $\text{Ir}_{0.7}\text{Ta}_{0.3}\text{O}_x$, due to the low electronic conductivity of Ta_2O_5 [2]. The catalytic activity for $\text{Ir}_{0.7}\text{Ta}_{0.3}\text{O}_x$ was still slightly higher than that of pure IrO_2 . It was previously suggested that an improved active surface area can be obtained when there is a proper ratio of Ir to Ta [36]. A similar trend in performance was reported by Hu *et al.* [33] however they observed a maximum current response at 30 mol% Ta content. Furthermore, a higher cell resistance was observed for the Ir-Ta oxides in comparison to other Ir based metal oxides [26]. The improved electrocatalytic activity observed by the addition of Ta_2O_5 to IrO_2 was probably as a result of the smaller particle sizes (revealed by XRD and TEM) and increased active surface sites (revealed by CV).

4. CONCLUSIONS

Electrocatalysts based on IrO₂ were successfully synthesised and characterised. CA analyses have shown that the addition of secondary metal oxides (RuO₂, SnO₂ and Ta₂O₅) to IrO₂, improved the catalytic activity of the oxide towards the OER. Ir_{0.7}Ru_{0.3}O₂, while displaying a slightly lower catalytic activity than Ir_(0.9)Sn_(0.1)O₂, proved to be the most promising electrocatalyst for the OER since no decrease in catalytic activity was observed as the RuO₂ content was increase up to 30 mol%. This suggests that even better catalytic activity may be achieved with even higher contents of RuO₂. The addition of SnO₂ and Ta₂O₅ was limited to 10 and 20 mol% respectively. CA proved to be a useful technique for the electrochemical characterisation of the electrocatalysts. TEM and XRD were useful in relating the physical structure of the electrocatalysts to the electrochemical activity. Particle sizes were found to be of nanometer scale for all the synthesised electrocatalysts thus rendering the Adams fusion method a relatively simple and quick method for directly producing metal oxides suitable as electrocatalysts for the SPE electrolyser. The combination of various metal oxides can be considered a viable approach to address the high cost and efficiency issues facing the present SPE electrolyser technology.

ACKNOWLEDGEMENTS

This work was supported by the South African Department of Science and Technology through the Technology Implementation Agency (TIA) project number T70600 (SPE Electrolyser).

References

1. W. Xu, J. Tayal, S. Basu, K. Scott, *Int. J. Hydrogen Energy*, 36 (2011) 14796.
2. A.T. Marshall, S. Sunde, M. Tsytkin, R. Tunold, *Int. J. Hydrogen Energy*, 32 (2007) 2320.
3. T. Maiyalagan, S. Pasupathi, *Mater. Sci. Forum*, 657 (2010) 143.
4. C. Xu, L. Ma, J. Li, W. Zhao, Z. Gan, *Int. J. Hydrogen Energy*, (2011) 1.
5. J. Cheng, H. Zhang, H. Ma, H. Zhong, Y. Zou, *Electrochim. Acta*, 55 (2010) 1855.
6. S. Song, H. Zhang, X. Ma, Z. Shao, R.T. Baker, B. Yi, *Int. J. Hydrogen Energy*, 33 (2008) 4955.
7. S. Siracusano, V. Baglio, A. Stassi, R. Ornelas, V. Antonucci, A.S. Arico, *Int. J. Hydrogen Energy*, 36 (2011) 7822.
8. J. Cheng, H. Zhang, G. Chen, Y. Zhang, *Electrochim. Acta*, 54 (2009) 6250.
9. E. Mayousse, F. Maillard, F. Fouda-Onana, O. Sicardy, N. Guillet, *Int. J. Hydrogen Energy*, 36 (2011) 10474.
10. A. Marshall, B. Børresen, G. Hagen, M. Tsytkin, R. Tunold, *Energy*, 32 (2007) 431.
11. A. Marshall, B. Børresen, G. Hagen, S. Sunde, M. Tsytkin, and R. Tunold, *Russian J. Electrochem.*, 42 (10) (2006) 1134.
12. R. Kötz, S. Stucki, *Electrochim. Acta*, 31 (10) (1986) 1311.
13. W. Xu, K. Scott, S. Basu, *J. Power Sources*, 196 (2011) 8918.
14. C. Angelinetta, S. Trasatti, *Mater. Chem. Phys.*, 22 (1989) 231.
15. E. Rasten, *Electrocatalysis in water electrolysis with solid polymer electrolyte*, PhD. Thesis, Norwegian University of Science and technology (2001).
16. J.M. Hu, H.M. Meng, J.Q. Zhang, C.N. Cao, *Corrosion Sci.*, 44 (2002) 1655.
17. Y. Zhang, C. Wang, Z. Mao, N. Wang, *Mater. Lett.*, 61 (2007) 1205.
18. R. Adams, R.L. Shriner, *J. Am. Chem. Soc.*, 45 (1923) 2171.

19. R.L. Shriner, R. Adams, *J. Am. Chem. Soc.*, 46 (1924) 1683.
20. E. Balko, C. Davidson, *J. Inorg. Nuclear Chem.*, 42 (1980) 1778.
21. A. Newkirk, D. McKee, *J. Catal.*, 11 (1968) 370.
22. A. Marshall, B. Børresen, G. Hagen, M. Tsykin, R. Tunold, *Mater. Chem. Phys.*, 94 (2005) 226.
23. C. Mallika, A.E.S. Raj, K. Nagaraja, O. Sreedharan, *Thermochim. Acta*, 371 (2001) 95.
24. S. Trasatti, G. Lodi, *Electrodes of conductive metallic oxides*, Elsevier Scientific Publishing Company, Amsterdam, (1980) 301.
25. J.M. Hu, J.X. Wu, H.M. Meng, D.B. Sun, Y.R. Zhu, D.J. Yang, *Trans. Nonferrous Metals Soc. China*, 10 (2000) 511.
26. A. Di Blasi, C. D'Urso, V. Baglio, V. Antonucci, A.S. Arico', R. Ornelas, F. Matteucci, G. Orozco, D. Beltran, Y. Meas, L. G. Arriaga, *J. Appl. Electrochem.*, 39 (2009) 191.
27. A. Marshall, B. Børresen, G. Hagen, M. Tsykin, R. Tunold, *Electrochim. Acta*, 51 (2006) 3161.
28. S. Ardizzone, C.L. Bianchi, L. Borgese, G. Capelletti, C. Locatelli, A. Minguzzi, S. Rondinini, A. Vertova, P.C. Ricci, C. Cannas, A. Musinu, *J. Appl. Electrochem.*, 39 (2009) 2093.
29. E. Slavcheva, I. Radev, G. Topalov, E. Budevski, *Electrochim. Acta*, 53 (2007) 362.
30. L.K. Xu, J.D. Scantlebury, *Corrosion Sci.*, 45 (2003) 2729.
31. CH. Comninellis, G.P. Verceci, *J. Appl. Electrochem.*, 21 (1991) 335.
32. L.M. Da Silva, D.V. Franco, L.A. De Faria, J.F.C. Boodts, *Electrochim. Acta*, 49 (2004) 3977.
33. J-M. Hu, J-Q. Zhang, *J. Mater. Sci.*, 38 (2003) 705.
34. C.P. De Pauli, S. Trassati, *J. Electroanal. Chem.*, 538 – 539 (2002) 145.
35. J. Xu, G. Liu, J. Li, X. Wang, *Electrochim. Acta*, 59 (2012) 105.
36. L. Bao-song, L. An, G. Fu-xing, *Trans. Nonferrous Metals Soc. of China*, 16 (2006) 1193.